Chapter 11

FFAG, Scaling

Abstract This chapter is an introduction to Fixed-Field Alternating Gradient (FFAG) cyclic accelerators, and to the theoretical material needed for the simulation exercises. It relies on charged particle optics and acceleration concepts introduced in the previous cyclotron and synchrotron chapters and further addresses
- design aspects of scaling FFAGs,
- beam dynamics in radial- and spiral-sector rings,
- synchrotron acceleration and various other acceleration techniques.

Simulations introduce dedicated keywords providing an analytical modeling of the field: FFAG (radial sector dipole) and FFAG-SPI (spiral sector). They otherwise use optical elements met in the previous chapters: DIPOLE[S], TOSCA, CAVITE, data input/output keywords such as FAISCEAU, FAISTORE, the SYSTEM keyword, etc. Beam dynamics simulations include

- particle trajectories through multiple-dipole FFAG cells,
- closed-orbit finding from multi-turn raytracing, or using FIT,
- finding dynamical aperture,
- deriving ancillary outcomes from rays, such as

  . transport matrices using MATRIX,
  . periodic optical functions and their transport using TWISS,
  . etc.

Notations used in the Text

A	sector angle of a dipole
$\mathbf{B}$; B_0	magnetic field at radius R; field value at reference radius R_0
$B_{\rm x,y,s}$	components of $\mathbf{B}$ in the moving frame
$B\rho$; $B\rho_0$	particle rigidity: $B\rho = p/q$; for reference momentum p_0
C; C_0	closed orbit length: $C = \oint ds = 2\pi\overline{R}$; for reference momentum p_0
ds	path length increment: $ds = Rd\theta$
E; E_{xtr}; E_{inj}; E_s	particle energy: $E = \gamma m_0 c^2$; at extraction; injection; synchronous
EFB	effective field boundary
f; $\mathcal{F}(\theta)$, $\mathcal{F}(r,\theta)$	flutter; field form factor
$f_{\rm rev}$, $f_{\rm rf}$	revolution and accelerating voltage frequencies
h	harmonic number, an integer, $h = f_{\rm rf}/f_{\rm rev}$
I_1	fringe field integral
k	geometric field index: $k = \frac{R}{B}\frac{\partial B}{\partial R} \approx -n\frac{R}{\rho}$
$\mathcal{L}$	magnetic length
m_0; m; M	particle rest mass; mass; mass in eV/c^2 units
N	number of cells in a ring
n	local focusing index: $n = -\frac{\rho}{B}\frac{\partial B}{\partial x}$
pf	packing factor: $pf = \mathcal{L}/C$
p; p_0; δp, Δp	particle momentum; reference momentum; offset
q	particle charge
R; R_0	radial coordinate, from center of ring; reference
$\overline{R}$	average closed orbit radius: $\overline{R} = C\ /\ 2\pi$
RF	Radio-Frequency: as per the accelerating voltage technology
s	path variable
v	particle velocity
$V_{\rm rf}$; $\hat{V}_{\rm rf}$	acceleration voltage; peak value
x, x’, y, y’	particle coordinates in the moving frame $[(*)' = d(*)/ds]$
Greek symbols	
α	momentum compaction, or trajectory deviation
$\beta = v/c; \beta_0; \beta_s$	normalized velocity; reference; synchronous
β_u, α_u, γ_u; $\eta_{\rm x,y}$	optical functions ($u = x,\ y,\ l$); dispersion function
γ	Lorentz factor: $\gamma = E/m_0c^2 = E[eV]/M$
δ	relative momentum offset: $\delta = \delta p/p$
ε	wedge angle
ϵ_R	strength of a depolarizing resonance
ε_u/π	Courant-Snyder invariant: $\gamma_u u^2 + 2\alpha_u uu' + \beta_u u'^2 = \varepsilon_u/\pi$
$\varepsilon_{\rm u,rms}$	beam emittance
ζ	spiral angle of a spiral sector dipole EFB
η	phase-slip factor
θ	local polar angle
κ	gap shape index
λ	fringe field extent
$\omega_{\rm rf}$	acceleration voltage angular frequency: $\omega_{\rm rf} = 2\pi f_{\rm rf}$
ρ	local curvature radius
φ	scalloping angle
ϕ_s	synchronous RF phase

11.1 Introduction

The Fixed field alternating gradient (FFAG) concept was devised in the early 1950's [1, 2, 3, 4]. Electrostatic accelerators, cyclotrons, betatrons, synchrotrons were part of the landscape at the time, as instruments for nuclear physics research, medical and industrial applications, X-ray generators, etc. Higher energies were driving accelerator technology R&D, and strong focusing, pulsed synchrotron cascades and collider rings on their way to take over. The FFAG concept was explored as an alternate implementation of strong focusing, liable to allow high intensity beams due to their - synchrocyclotron-like - capability of very fast cycling allowed by the fixed magnetic field, and to the large momentum and geometrical acceptance of strong focusing scaling FFAG optics and magnets. Three electron models were built and operated in the 1953-1967 period, by the Midwestern Universities Research Association [1]. These early FFAG studies produced a wealth of theoretical and computational contributions to beam theory and beam manipulation in cyclic accelerator magnets and RF systems.

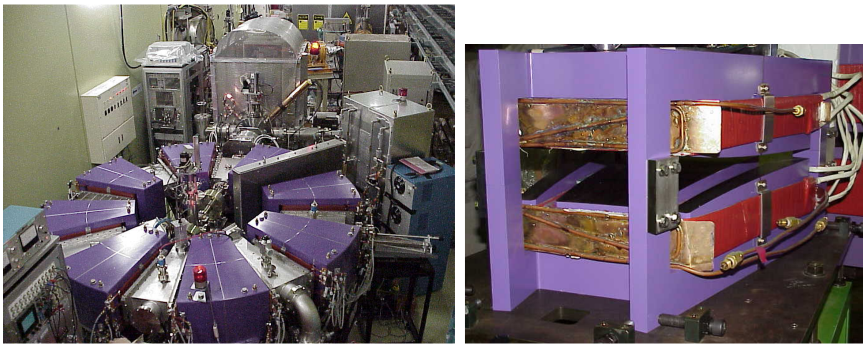

Fig. 11.1 Left: PoP, the first proton FFAG, a 500 keV Proof-of-Principle 8-period ring operated at KEK from 1999 on [5]. Beam delivered by the 50 kV H^+ source (seen behind the ring) is steered across the ring vacuum chamber onto the inner radius injection orbit. The high gradient RF cavity can be seen between two dipole triplets to the right, with its power supply to its right. Right: dipole-triplet cell; injection orbit is in the wide gap region, extraction orbit in the narrow gap region

The interest in FFAG technologies resurrected in the late 1990s in the context of high energy physics R&D programs and the acceleration of short-lived beams, with potential spin-offs including medical accelerators and high power proton and electron beam accelerators [6, 7, 8] (Fig. 11.1). Several proton and electron machines were built in Japan from the 1990s on [6], including a prototype ADS-Reactor installation, and other internal target and beam cooling experiments [9, 10]. A prototype of a FFAG spiral sector dipole was later built as part of a multiple-beam protontherapy ring design study [11] (Fig. 11.2).

Orbits spiral out in FFAGs during acceleration, as a consequence of the fixed magnetic field, as in cyclotrons and synchrocyclotrons. FFAGs optics is non-isochronous:

Fig. 11.2 Prototype, full scale, and pole, of the spiral sector dipole of a 200 MeV proton therapy scaling FFAG design [11]

the radial field index k is constant to ensure constant tunes as the beam spirals out (isochronism requires $k = \beta^2\gamma^2, seeChapt.\ 5, Eq.\ 5.1$). FFAGs are normally operated as synchrocyclotrons: the RF is cycled, voltage frequency modulated during the ramp; repetition rates of 10s of kHz are potentially achievable with today's RF system technologies. High power and fast acceleration R&D have produced alternate acceleration and RF manipulation techniques, including quasi-isochronous optics and CW acceleration [12, 13, 14, 15, 16].

11.2 Basic Concepts and Formulæ

Consider Hill's equations

$$\left\{ \begin{aligned} &\frac{d^2x}{d\theta^2} + \frac{R^2}{\rho^2}(1-n)x = 0 \\ &\frac{d^2y}{d\theta^2} + \frac{R^2}{\rho^2}ny = 0 \end{aligned} \right. \tag{11.1}$$

(these equations assume that orbit scalloping is marginal, *i.e.* a quasi-circular closed orbit [17]). At a given angle θ in an FFAG sector, constant radial and axial focusing is equivalent to

$$\frac{d}{dp}\left((1-n)\frac{R^2}{\rho^2}\right)\bigg|_\theta = 0 \quad \text{and} \quad \frac{d}{dp}\left(n\frac{R^2}{\rho^2}\right)\bigg|_\theta = 0 \tag{11.2}$$

A sufficient condition for Eq. 11.2 is

$$\left.\frac{\partial}{\partial p}\left(\frac{R}{\rho}\right)\right|_{\theta} = 0 \qquad \text{and} \qquad \left.\frac{\partial n}{\partial p}\right|_{\theta} = 0 \tag{11.3}$$

The first condition yields constant ratio *particle radial position / local curvature radius*: the geometrical scaling property, orbits of different momenta scale with energy, the center of similitude is the center of the ring. The second condition yields momentum-independent local focusing index: the zero-chromaticity property.

Geometrical similarity results in a constant geometrical field index

$$k = \frac{R}{B(R)} \left.\frac{\partial B(R)}{\partial R}\right|_{R} = -\frac{R}{\rho} n = \mathit{constant} \tag{11.4}$$

which, by integration, yields the R-dependence of the field in an FFAG dipole,

$$B(R) = B_0 \left(\frac{R}{R_0}\right)^{k} \tag{11.5}$$

From $k = \mathit{constant}$ (Eq. 11.4) it results that reversing the sign of the curvature radius ρ reverses the sign of the field index n. Radial FFAG lattices combine such alternating index dipoles, Fig. 11.3 and Sect. 11.2.1. A way to obtain such radial field distribution is by shaping the dipole gap, following

$$g(R) \approx g_0 \left(\frac{R_0}{R}\right)^{\kappa} \qquad \text{with } \kappa \approx k \tag{11.6}$$

with greater (lower) gap at lower (greater) energy and radius (Fig. 11.3). Another way is by distributed current coils along the poles of a parallel gap dipole [1, 18, 19]. More generally, in a lattice comprised of bends and field-free sections, the magnetic field along an orbit in the median plane (y=0) satisfies

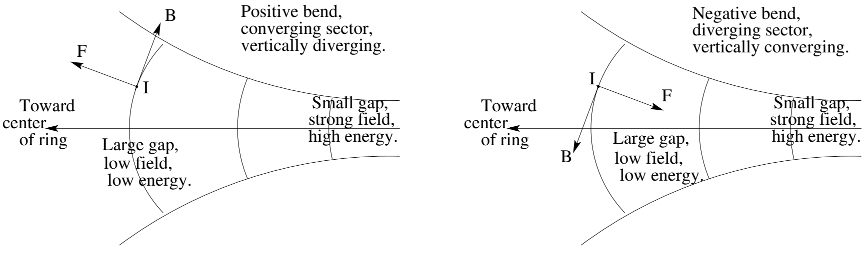

Fig. 11.3 Focusing and defocusing FFAG sectors

$$B(R,\theta) = B_0 \left(\frac{R}{R_0}\right)^{k} \mathcal{F}(R,\theta) \tag{11.7}$$

where the $2\pi/N$-periodic flutter factor $\mathcal{F}(R,\theta)$ describes the azimuthal variation of the field along an orbit (in a similar way to the modeling of the AVF cyclotron, Chap. 5, Eqs. 5.4, 5.10). A flutter can be defined and quantifies the departure of the azimuthal variation of the field from a step function (Eq. 5.5).

Orbits

It results from the scaling field (Eq. 11.5) that the average orbit radius and the orbit length satisfy the momentum dependence, respectively,

$$\frac{R(p)}{R_0} = \left(\frac{B\rho}{B\rho_0}\right)^{1/(k+1)} = \left(\frac{p}{p_0}\right)^{1/(k+1)} \quad \text{and} \quad C(p) = C_0\left(\frac{p}{p_0}\right)^{\frac{1}{k+1}} \tag{11.8}$$

The R- and ρ-radius arcs share a common cord (Fig. 11.4), which writes

$$R\sin(A/2) = \rho\sin(\pi/N) \tag{11.9}$$

A packing factor can be defined,

$$pf = \frac{\text{magnetic length}}{\text{orbit length}} = \frac{\mathcal{L}}{C} = \frac{N\times A}{2\pi} \tag{11.10}$$

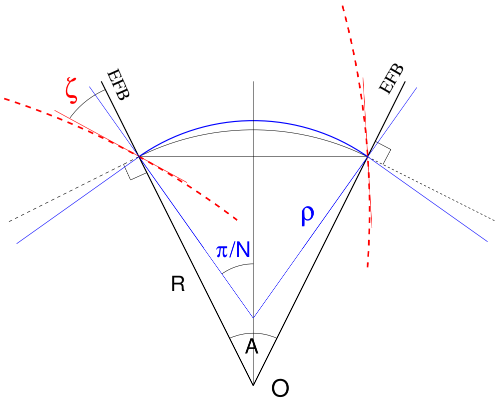

Fig. 11.4 Geometrical parameters in a radial (straight EFBs) or spiral (dashed lines; spiral angle ζ) FFAG sector dipole. O is the center of the ring and the EFBs form a sector angle A. The R-radius arc is a line of constant field (Eq. 11.5). The closed orbit is approximately along the ρ-radius arc. Both arcs share the same cord

In a general manner, closed orbits have to be computed numerically, searching for the momentum-dependent closed solution over a period. They feature small amplitude scalloping in the vicinity of an average circular path with radius $R(p)$ (Eq. 11.8), thus the initial radius value for a numerical search can be taken as $R \approx R(p)$, whereas the incidence dR/ds is null with proper choice of the origin.

The orbit excursion, from injection momentum to extraction momentum, satisfies (Eq. 11.8)

$$R_{xtr} - R_{inj} = R_0 \left(1 - \left(\frac{p_{inj}}{p_{xtr}}\right)^{\frac{1}{1+k}}\right) \tag{11.11}$$

Focusing

There is two ways that the FFAG technique implements strong focusing,

- one consists in alternating strong transverse gradients (large $|n|$, Eq. 11.4), which is achieved by alternating positive- and negative-bend magnets (Sect. 11.2.1), with the detrimental effect of increased circumference of the ring (Eq. 11.8) and decreased packing factor (Eq. 11.10);

- a second method consists in using positive bend only, and rely on spiral EFBs and Thomas (AVF) focusing: a large spiral angle (strong axial focusing, radially defocusing) compensates the large field index (strong radial focusing, axially defocusing). A logarithmic spiral edge [3] has the virtue of ensuring constant wedge angle (Sect. 11.2.2).

Fringe fields may have a noticeable effect on the effective axial focusing (Sect. 18.3.1): Eq. 18.20 indicates that, in the case of constant wedge angle (spiral scaling dipoles), the axial focusing correction for the fringe field extent, ψ, is constant *iff* $\lambda \propto R$, which requires λ (a measure of the the gap height) to increase linearly with radius. In the gap shaping method (Eq. 11.6) the gap decreases with radius instead (Figs. 11.1, 11.3), thus leading to an increase in axial wave number with energy: overcoming that effect requires proper counter-measures such as for instance a specific design of the chamfers, and field clamps [20].

Wave numbers

The cyclotron approximations to the radial and axial wave numbers (Sects. 5.2.1, 5.2.2) still hold, namely

$$\nu_R \approx \sqrt{1+k}, \quad \nu_y \approx \sqrt{-k + F^2(1 + 2\tan^2\zeta)} \tag{11.12}$$

with $\zeta = 0$ in the case of a radial sector. These approximations, not necessarily accurate, are helpful in evaluating the relative effects of a small change of value of the flutter F, of the geometrical field index k, or of the spiral angle ζ in addition in the case of a spiral sector.

11.2.1 Radial Sector

A radial sector scaling FFAG facility is displayed in Fig. 11.5 [21]: a 150 MeV ring built and operated at KEK in the early 2000s. The ring is comprised of 12 Defocusing-Focusing-Defocusing (DFD) dipole triplets. The radial dependence of

Fig. 11.5 Left: A 150 MeV 12-cell scaling FFAG ring, and its cyclotron injector [5]. Right: Its lattice cell magnet, a DFD dipole triplet. The gap shape follows Eq. 11.6 so ensuring the scaling field law (Eq. 11.5) [21]

Table 11.1 Design parameters of the a radial sector 150 MeV proton scaling FFAG.

Injection - extraction energy	MeV	12 - 150
Injection - extraction radius	m	4.7 - 5.2
Lattice		DFD
Number of cells (N)		12
Maximum β_R; β_z max.	m	3.8; 1.3
Wave Numbers, ν_R; ν_z		3.7; 1.2
Magnet		
Type		radial sector DFD triplet
Sector angle A_D; A_F	deg	3.43; 10.24
Injection - extraction gap height	cm	20 - 4
Scaling index $k_D = k_F$		7.6
B_D; B_F, at 150 MeV	T	-1.21745; 1.69056
Acceleration		
Frequency swing	MHz	1.5 - 4.6
Harmonic		1
Voltage, peak-to-peak	kV	19
Cycle time	ms	4
Maximum repetition rate	Hz	250
Equivalent dB/dt	T/s	280
Synchrotron tune ν_s		0.039 - 0.012

the magnetic field in the D and F sectors satisfies Eq. 11.5, as a result of a gap shape following Eq. 11.6 (as in the prototype PoP dipole, Fig. 11.1). The main parameters of the ring are summarized in Table 11.1.

Hall-probe measurements of an isolated dipole triplet are displayed in Fig. 11.6. Mutual influence in the ring actually produces a 200 Gauss field across the drift between two triplets: Fig. 11.6 shows the field from OPERA computation in the periodic hypothesis [22].

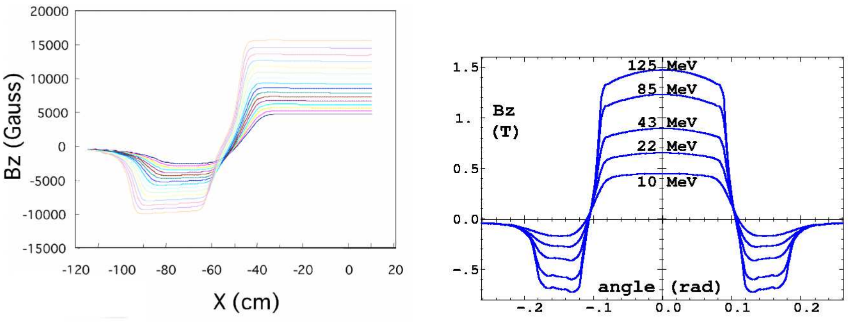

Fig. 11.6 Left: measured vertical magnetic field $B_Z(X)$, along R=constant arcs across one half of the radial sector dipole triplet [21]. The X coordinate is along an axis normal to the vertical symmetry plane of the triplet (the X=0 plane). The field on the plateau accurately follows the r^k scaling law (Eq.11.5), lower (greater) field at lower (greater) energy, greater (lower) dipole gap. Right: field along the periodic orbits across the cell at various energies (proton), from an OPERA field map of the KEK FFAG dipole triplet cell [22]

Transverse acceptance

Scaling FFAG optics features large dynamical transverse acceptance [23], see the case of KEK FFAG ring in Fig. 11.7.

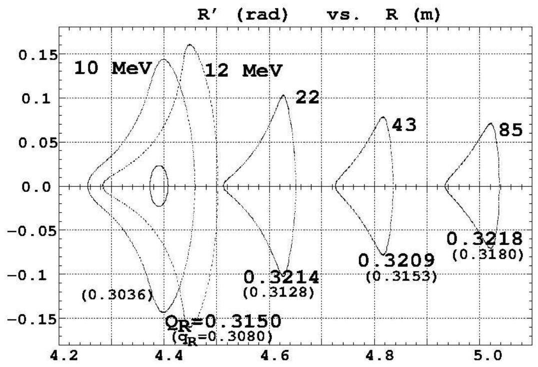

Fig. 11.7 Radial motion 1,000-turn stability limit at various energies. The small ellipse within the 10 MeV stability invariant on the left is for a nominal $\varepsilon_R = 0.04\,\pi$cm beam at injection energy. The single-cell radial wave number at stability limit (Q_R) and paraxial (q_R, between parentheses) give an idea of the amplitude detuning [22]

11.2.2 Spiral Sector

A typical design of a spiral sector scaling FFAG is shown in Fig. 11.8: a variable energy and multiple extraction 230 MeV ring, aimed at cancer tumor treatment [24, 25]. Table 11.2 summarizes the parameters of the FFAG magnet and ring. The ring

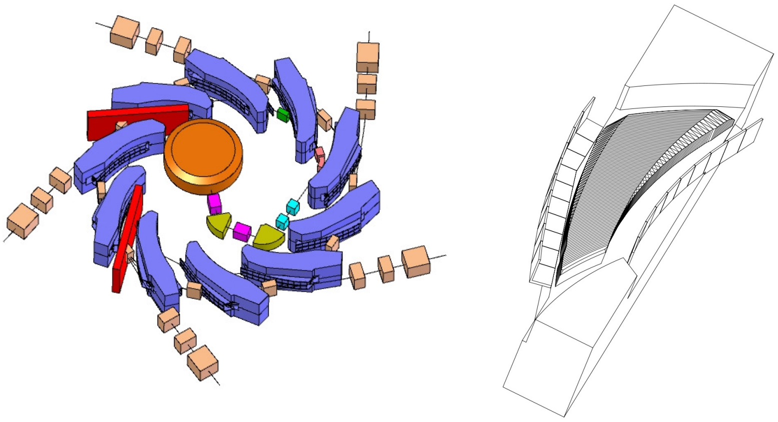

Fig. 11.8 Left: RACCAM proton therapy scaling FFAG ring design, including a variable energy H^- cyclotron injector. Right: a scheme of its spiral dipole half-yoke, showing the gap shaping pole piece with its variable width chamfers and the EFB field clamps, two features that result in quasi-constant axial wave number [24]. The EFB has a constant spiral angle $\zeta = 53.7^o$

Table 11.2 Design parameters of the RACCAM proton therapy spiral sector scaling FFAG ring. Some of the parameter values vary with variable operation energy: values given here concern the extraction energy range 70 to 180 MeV

		Injection	Extraction
energy, variable	MeV	5.55 → 15	70 → 180
$B\rho$	T.m	0.341 → 0.562	1.231 → 2.030
$B\rho_{\text{extr.}}/B\rho_{\text{inj.}}$		3.612	
$\beta\gamma$		0.109 → 0.180	0.393 → 0.648
Lattice type		spiral, scaling	
Number of cells (N)		10	
Packing factor (pf)		0.34	
Drift length	m	1.15	1.42
Orbit radius (R)	m	2.794	3.460
Orbit excursion (Eq. 11.8)	m	0.667	
Wave Numbers ν_R (constant); ν_y		2.76; 1.55 → 1.60	
Transition gamma (γ_{tr})		2.45	
Magnet			
Type		spiral sector	
Sector angle (A)	deg.	12.24	
Spiral angle (ζ)	deg.	53.7	
Scaling index k		5	

is comprised of 10 spiral sector cells. The radial dependence of the magnetic field in the spiral dipole satisfies Eq. 11.5 and results from the gap shape which follows Eq. 11.6. The dipole can be operated up to 2 T on the extraction radius, corresponding to 230 MeV extraction energy [20, 26]. Hall-probe field measurements are displayed in Fig. 11.9, together with fields from OPERA computation which are in accord

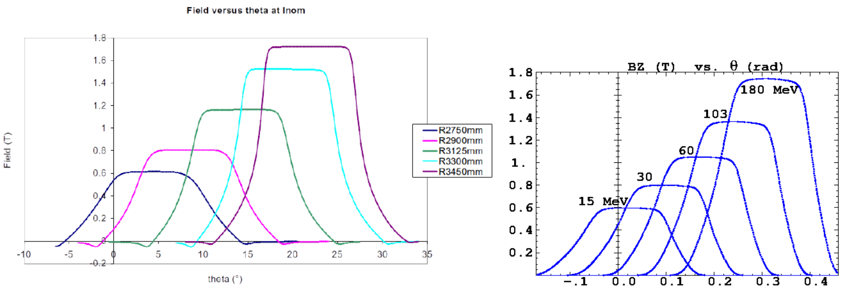

Fig. 11.9 Left: measured vertical magnetic field $B_Z(\theta)$, along R=constant arcs across RACCAM spiral sector dipole [26]. The field on the plateau satisfies the R^k scaling law (Eq.11.5), lower (greater) field at lower (greater) energy, greater (lower) dipole gap. Right: field along closed orbits across the dipole, from OPERA field map computations

within a few percent.

Constant wedge angle

A spiral EFB ensures constant wedge angle and thus R-independent focusing, while compensating the axially defocusing effect of a strong field index (Eq. 11.12). A spiral sector field boundary is defined by

$$\theta - \tan\zeta \, \ln\frac{R}{R_0} = \mathit{constant}, \qquad \mathit{i.e.}, \qquad R = R_0 \exp\left(\frac{\theta}{\tan\zeta}\right) \tag{11.13}$$

Note that an $\frac{R}{R_0}$-homothety, $\frac{2\pi}{N}$-rotation orbit similarity results (which reduces to a simple homothety in a radial lattice as $\zeta = 0$). The median plane field in a spiral sector can be written under the form

$$B(R,\theta) = B_0 \left(\frac{R}{R_0}\right)^k \mathcal{F}\left(\tan\zeta \, \ln\frac{R}{R_0} - \theta\right) \tag{11.14}$$

wherein $\mathcal{F}\left(\tan\zeta \, \ln\frac{R}{R_0} - \theta\right)$ is a $\frac{2\pi}{N}$-periodic function of θ. A convenient model for the azimuthal modulation assumes a sinusoidal dependence of the field,

$$\mathcal{F}(R,\theta) = 1 + f \sin\left(N\left(\tan\zeta \, \ln\frac{R}{R_0} - \theta\right)\right) \tag{11.15}$$

Transverse acceptance

Spiral sector scaling FFAG optics features large dynamical transverse acceptance. As an illustration of that property, the radial dynamical acceptance of RACCAM spiral sector FFAG ring (Fig. 11.8) is displayed in Fig. 11.10. The latter has been obtained from raytracing in a theoretical field model built from the EFB geometry and the R^k dependence of the field, whereas the azimuthal dependence is modeled using Eq. 11.7 and Enge's style fall-off (Eq. 18.14) [25].

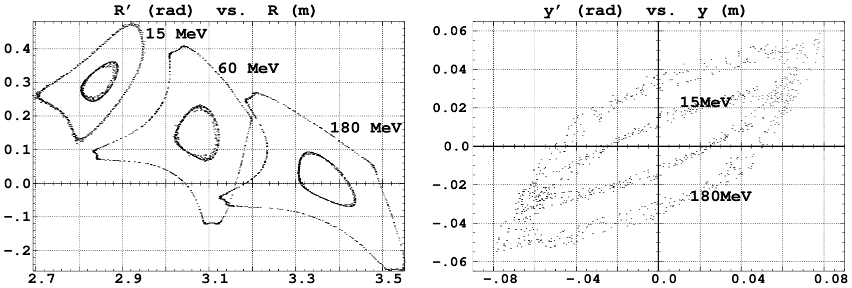

Fig. 11.10 The large stability limit (1,000-turn), at various energies, in a spiral sector FFAG. Left: radial motion; the outer invariants are for pure radial motion, they are several $10^3\,\pi$mm mrad. inner invariants are the stability limit in the presence of small amplitude axial motion, dynamical acceptance decreases to $\approx 10^3\,\pi$mm mrad, an effect of non-linear coupling. Right: 15 MeV case (inner, elliptical shaped distribution) and 180 MeV case (outer distribution); the dynamical acceptance is about 600 πmm mrad and 2000 πmm mrad, respectively

11.2.3 Longitudinal motion, acceleration

Given the orbit length (Eq. 11.8), the revolution period can be written

$$T_{\rm rev} = \frac{C}{\beta c} = T_{\rm rev,0}\left(\frac{p}{p_0}\right)^{\frac{1}{k+1}}\frac{\beta_0}{\beta} = T_{\rm rev,0}\left(\frac{p}{p_0}\right)^{\frac{-k}{k+1}}\frac{E}{E_0} \qquad (11.16)$$

The momentum compaction and transition γ write, respectively,

$$\alpha = \frac{\Delta C/C}{\Delta p/p} = \frac{1}{1+k} \quad \text{and} \quad \gamma_{tr} = \sqrt{1/\alpha} = \sqrt{1+k} \qquad (11.17)$$

Longitudinal focusing and synchronous acceleration in a scaling FFAG proceed as in synchro-cyclotrons, (Chap. 8), the synchrotron frequency is given by Eq. 8.4, the momentum acceptance of the lattice is given by Eq. 8.7.

A practical injection to extraction cycle includes single-bunch or multiturn injection, RF capture, synchronous acceleration, and single-turn kicker-septum extraction. Fixed-field allows fast cycling, with repetition rate up to hundreds of Hz provided an appropriate amount of accelerating voltage.

Other modes of acceleration have been devised as part of FFAG studies, with various goals such as fast acceleration of short-lived particles, high average current, rapid phase rotation. Several have been subject to a proof-of-principle, including quasi-synchronous serpentine acceleration [12], bucket acceleration [13, 14], multiple-bunch acceleration by multiple RF wave [15], longitudinal phase rotation [16]. induction acceleration using a betatron core [18], hybrid betatron-synchrotron acceleration [27, 28], harmonic-jump [14].

Betatron damping

In the presence of acceleration the equations of transverse motion write [29]

$$\left\{\begin{aligned} & x'' + \frac{(\gamma\beta)'}{(\gamma\beta)}x' + \frac{1-n}{\rho^2}x = 0 \\ & y'' + \frac{(\gamma\beta)'}{(\gamma\beta)}y' + \frac{n}{\rho^2}y = 0 \end{aligned}\right. \tag{11.18}$$

In the adiabatic approximation (slow damping, compared to betatron frequency) the solutions can be written

$$\begin{matrix} x(s) \\ y(s) \end{matrix} = \frac{1}{\sqrt{|h_{\substack{x\\y}}|}}\frac{1}{\sqrt{\beta\gamma}}\left[A_{\substack{x\\y}}\exp\left(\int h_{\substack{x\\y}}\,ds\right) + B_{\substack{x\\y}}\exp\left(-\int h_{\substack{x\\y}}\,ds\right)\right] \tag{11.19}$$

with

$$\left.\begin{aligned} h_x^2(s) &= -\frac{1-n}{\rho^2} \\ h_y^2(s) &= -\frac{n}{\rho^2} \end{aligned}\right\} + \frac{1}{2}\frac{d}{ds}\left[\frac{(\gamma\beta)'}{(\gamma\beta)}\right] + \frac{1}{4}\left[\frac{(\gamma\beta)'}{(\gamma\beta)}\right]^2 \tag{11.20}$$

and $A_{\substack{x\\y}}$ and $B_{\substack{x\\y}}$ constants depending upon the initial conditions. Considering that $\rho \propto R$ (Eq. 11.4), assuming stable periodic motion, and dropping the $(\beta\gamma)'$ terms in Eq. 11.20 (h(s) slowly varying), it results from Eq. 11.19 that the transverse particle oscillations satisfy

$$x, y \propto \frac{\sqrt{R}}{\sqrt{\beta\gamma}}, \qquad x', y' \propto \frac{1}{\sqrt{R}\sqrt{\beta\gamma}} \tag{11.21}$$

thus the damping of betatron oscillations is R-dependent. An invariant ensemble average results,

$$\beta\gamma\,\varepsilon_{rms} = \beta\gamma\,\left[< x^2 >< x'^2 > - < xx' >^2\right]^{1/2} = \text{ constant} \qquad (11.22)$$

i.e., betatron damping of the transverse emittances $\varepsilon_{rms} \propto 1/\beta\gamma$.

11.3 Exercises

The following exercises address the two types of scaling FFAG lattices discussed above: radial sector and spiral sector. Because scaling optics dipoles have a wide gap, fringe field extent and overlapping may be a concern: the technique described in Sect. 18.2.6 is used to handle this aspect of the optics.

11.3.1 A 150 MeV, Proton, Radial Sector FFAG

The 150 MeV radial sector FFAG operated at KEK in the early 2000 (Fig. 11.5) is the subject of the simulations in this series of exercises. Its parameters are given in Tab. 11.1 [21], the cell geometry is sketched in Fig. 11.11, the ring geometry and a few orbits (an outcome of the present exercises) are displayed in Fig. 11.12.

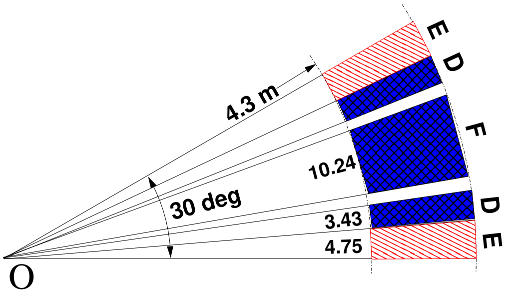

Fig. 11.11 Geometry of a 30 degree DFD cell. The center of the ring is at O. F and D are the focusing and and defocusing sectors of the dipole triplet, respectively 10.24 degree and 3.43 degree. The shadowed 4.75 degree "E" regions represent a half of the interval between two dipole triplets, a region of ≈ 200 G stray field [22, 30]

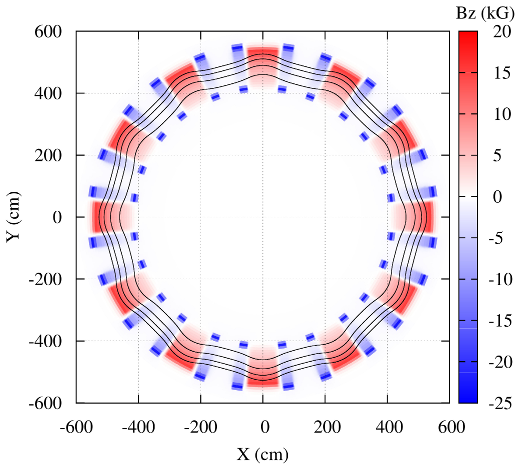

Fig. 11.12 A sketch of KEK 150 MeV FFAG ring, and a few closed orbits obtained using the keyword FFAG in zgoubi. A graph obtained using gnuplot: geometrical data taken from zgoubi.dat, orbit coordinates are read from zgoubi.plt [29]

11.1 Field in a Radial Sector Dipole Triplet

Solution: page 401.

The FFAG keyword is based on Eqs. 11.7 and 18.18 to provide the combined field from N neighboring dipoles, at particle location during the stepwise integration of motion. The field flutter factor $\mathcal{F}_i(R,\theta)$ (Eq. 18.18) is based on the fringe field model described in Sect. 18.2.6 (Eq. 18.14).

(a) Using FFAG keyword, and accounting for the magnet and cell parameters of Tab. 11.1, produce an input data file for the simulation of a cell.

(b) Produce a graph of the median plane field $B_Z(R,\theta)$ in the dipole triplet. The keyword OBJET[KOBJ=1] can be used to generate a dense set of parallel trajectories in the median plane, and OPTIONS[CONSTY=ON] to force them on constant radii as they are pushed through the dipoles. Use option FFAG[IL=2] for a record of step by step trajectory data in zgoubi.plt. Field data can be read from the latter, to produce a 2D graph of the field $B_Z(R,\theta)$.

(c) While we are here... Using the process in (b) it is possible to generate a mid-plane field map, on an even 2D meshing, which TOSCA in turn can use and track through. This requires (i) proper particle sampling for constant ΔR between trajectory arcs so ray-traced, (ii) proper integration step size FFAG[XPAS] to cover in an evenly fashion the 30 degree angular sector.

Field data can subsequently be read from zgoubi.plt and re-written in a field map ascii file with proper formatting for TOSCA to handle.

Work this out, and re-do question (b) to check the identity of the raytracing outcomes.

11.2 Orbits, Scalloping

Solution: page 403.

The input data file of exercise 11.1 can be used as a starting point in this exercise.

(a) Compute a scan of the periodic orbits $R(\theta)$ across the cell, for a few proton energies ranging in $12 \leq E \leq 200$ MeV. REBELOTE can be used to loop on the energy (by changing the relative particle rigidity D under OBJET), preceded by FIT to find the periodic orbit at the energy of concern.

Give a graph of these orbits $R(\theta)$, and on a separate graph the field $B(\theta)$ along the orbits. These data can be read from zgoubi.plt, filled using FFAG[IL=2].

(b) Give a graph of the previous orbits around the ring. Show graphically that these orbits are similar, check the similarity ratio.

(c) By tracking, show that orbit excursion over an energy range $12 \leq E \leq 200$ MeV (average radius spans from R_{inj} to R_{xtr}), satisfies Eqs. 11.8, 11.11. Particle coordinates at some azimuth along the ring can be logged in that aim in zgoubi.res using FAISCEAU (a linux "grep" can then grab them for plotting), or in an ancillary zgoubi.fai file using FAISTORE.

(d) Evaluate the orbit scalloping, *i.e.*, the maximum value of $|R(\theta) - R|/R$. Give a graph of the latter as a function of energy.

11.3 Zero-Chromaticity

Solution: page 406.

This exercise investigates the momentum dependence of the wave numbers.

(a) Compute and give a graph of the momentum dependence of the radial and axial wave numbers in the 12-cell ring (Fig. 11.5). Use for that either one of the following two methods to obtain the wave number values:

(a.1) From the cell transport matrix, using MATRIX. REBELOTE can be used in that case to repeat on momentum values.

(a.2) from Fourier analysis of small amplitude motion.

Compare the results with theory (Eq. 11.12).

(b) It can be observed that the radial wave number is constant with momentum/orbit radius R, this is expected from the scaling law (Eq. 11.5); however the axial wave number is R-dependent.

In the field model, introduce a R-dependence of the gap of the form Eq. 11.6: this is equivalent to introducing an R-dependence of the fringe field extent, or equivalently of the field form factor $\mathcal{F}(\theta)$ (Eq. 11.7), proper to change the R-dependence of the axial focusing. Find the value of κ which minimizes the change of ν_y over the energy interval $12 \leq E \leq 150$ MeV, provide a simulation to show the efficiency of the method.

(c) Compute the value of the momentum compaction and transition γ_{tr} at two sample energies, 12 and 150 MeV. TWISS can be used for that, with OBJET[KOBJ=5]. Check their relationship to the radial wave number.

11.4 Beam Envelopes; Phase Space

Solution: page 410.

(a) Produce a graph of the trajectories of a beam bundle across the cell, at 12 and 150 MeV. Take initial coordinates evenly distributed on initial paraxial invariants. OBJET[KOBJ=8] can be used to define that set of particles.

(b) Perform single particle tracking, over many turns, using REBELOTE. Consider two cases, separately: paraxial motion, and large excursion motion. Show that large excursion phase space motion features non-linear coupling.

11.5 Acceleration: Transverse Betatron Damping

(a) Produce a simulation of the transverse and longitudinal motions of a particle taken on a small initial invariant, over a $10 \rightarrow 150\,$MeV acceleration cycle in the 12-cell ring. Assume the following RF parameters: peak voltage $\hat{V} = 40\,$kVolts, synchronous phase $\phi_s = 20^o$, harmonic h=1. Acceleration uses CAVITE[IOPT=6], which imposes defining the particle type, with PARTICUL; multiturn is obtained using REBELOTE. SCALING takes care of having magnetic fields ramped to follow momentum increase by CAVITE.

(b) Show graphically that the transverse betatron oscillation damping satisfies the R-dependence of Eq. 11.21.

(c) Accelerate a bunch of a few tens of particles. Check the beam emittance damping of Eq. 11.22.

11.3.2 RACCAM Proton Therapy Spiral Sector FFAG

This series of exercises is based on the 180 MeV spiral sector FFAG design of Fig. 11.8. The parameters of concern are given in Tab. 11.2 [20, 24, 25, 26]. The cell geometry is sketched in Fig. 11.13.

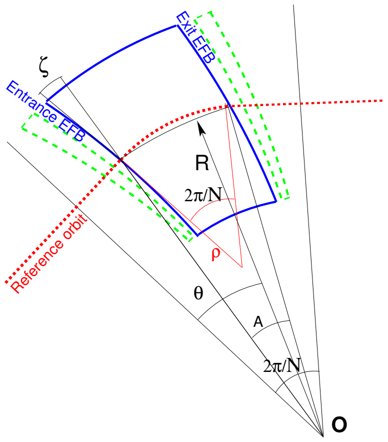

Fig. 11.13 A sketch of RACCAM spiral sector dipole and $2\pi/10$ cell. O is the center of the ring and the EFBs form a sector angle A. Note that the reference orbit is not strictly circular, the bending radius is not constant along the trajectory over the $2\pi/N$ arc (a line of constant field is an R-radius arc, centered on O).

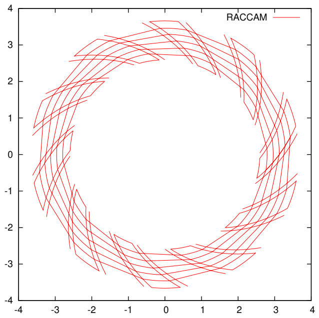

Fig. 11.14 A simulation of RACCAM FFAG ring in zgoubi, including a few orbits, using the keyword FFAG-SPI. A graph obtained using gnuplot, geometrical data taken from zgoubi.dat, and particle data read from zgoubi.plt

11.6 Field in a Spiral Sector Dipole

The FFAG-SPI keyword is based on Eq. 11.14 to generate the field from a spiral sector dipole (or several sectors side-by-side within an AT angular extent [31, Sect. FFAG-SPI]) at particle location, while motion proceeds across the magnet. FFAG-SPI has provision for the modeling of the azimuthal form factor $\mathcal{F}_i(R,\theta)$, and the overlapping of neighboring fringe fall-offs, based on the method described in Sect. 18.2.6.

(a) Using FFAG-SPI keyword, produce a graph of the median plane field $B_Z(R, \theta)$ in RACCAM spiral sector dipole. OBJET[KOBJ=1] can be used to generate a trajectory sample, and OPTIONS[CONSTY=ON] to force these trajectories on constant radii. Option FFAG-SPI[IL=2] will log in zgoubi.plt the step by step trajectory field data; the latter can subsequently be plotted.

(b) CYCLOTRON keyword could be used as well: it allows some sophistication in field modeling compared to using FFAG-SPI, such as accounting for an R-dependence of the geometrical field index k (a capability which is used in exercise 5.6 - Relativistic Cyclotron Chapter, to adjust the isochronism), and of the fringe field extent, via an R-dependent gap shape index $\kappa(R)$ in Eq. 11.6.

Move the FFAG modeling of (a) to CYCLOTRON. Try some radial dependence of both k and of fringe extent, with the constraint of maintaining constant radial and axial tunes over the spiral orbit radial excursion. FIT can be used for this optimization of tune constancy.

(c) While we are here... Using the process in question (a), it is possible to generate a mid-plane field map, on an even 2D meshing, which TOSCA in turn can use and track through. This requires (i) proper particle sampling in OBJET for constant ΔR between trajectory arcs so ray-traced, (ii) proper integration step size FFAG[XPAS] to cover in an evenly fashion the 30 degree angular sector.

Field data can subsequently be read from zgoubi.plt and logged in a field map file with proper formatting for TOSCA to handle.

Work this out, and re-do question (b) using TOSCA, to check the identity of the raytracing outcomes with the CYCLOTRON case.

11.7 Orbits, Scalloping

Characterizing the focusing properties of the lattice (say, over the radial span of the accelerated orbit) first requires finding the periodic orbits over that radial extent. The radius - or momentum - dependence of optical functions may then be found (exercise 11.9), as well as the radius dependence of time of flight for further acceleration (exercise 11.14), etc.

(a) Compute a scan of the periodic orbits $R(\theta)$ across the cell, for a few proton energies ranging in $15 \leq E \leq 180$ MeV. REBELOTE can be used to loop on the energy (by changing the relative particle rigidity D under OBJET), preceded by FIT to find the periodic orbit at the energy of concern.

Give a graph of these orbits $R(\theta)$, and on a separate graph the field $B(\theta)$ along the orbits. These data can be logged in zgoubi.plt during ray-tracing, using FFAG-SPI[IL=2].

(b) Show graphically the homothety-rotation of the orbits.

(c) By tracking, show that orbit excursion over an energy range $15 \leq E \leq 180$ MeV (average radius spans from R_{inj} to R_{xtr}), satisfies Eqs. 11.8, 11.11.

11.8 Zero-Chromaticity

(a) Compute and give a graph of the momentum dependence of the radial and axial wave numbers in the 10-cell ring (Fig. 11.8). Use for that either one of the following two methods to obtain the wave number values:

(a.1) from the cell transport matrix,

(a.2) from Fourier analysis of paraxial motion.

Compare with expectations (Eq. 11.12).

(b) It can be observed that the radial wave number is constant with momentum, or equivalently with the orbit radius R, this is expected from the scaling law (Eq. 11.5). However the axial wave number is R-dependent. Explain why.

(c) In the field model, introduce a R-dependence of the gap of the form Eq. 11.6. Note: this is equivalent to introducing a R-dependence of the fringe field extent, or equivalently of the field form factor $\mathcal{F}(\theta)$ (Eq. 11.7), proper to change the R-dependence of the axial focusing. Using the FIT procedure, compute the value of κ which minimizes the change of ν_y over the energy interval $15 < E < 180$ MeV.

(d) Compute the value of the momentum compaction and transition γ_{tr}, at 12 and 150 MeV. Check their relationship to the radial wave number.

11.9 Beam Envelopes, Optical Functions

Produce graphs of radial and axial beam bundles across the cell, at 15 and 180 MeV. Derive from these the envelope values and the betatron function amplitudes.

11.10 Periodic Stability Domain

Vary the scaling index k and spiral angle ζ of the spiral dipole, in FFAG-SPI:

- produce a two-dimensional (ν_R, ν_y) wave number scan diagram, covering the motion stability area resulting from varying k and ζ.
- produce the corresponding (k, ζ) stability limit diagram.

11.11 Motion Stability Limit

Tracking single particle radial motion in the OPERA field map of the FFAG dipole triplet, yields at stability limit the phase space portrait of Fig. 11.15 [22]. Re-produce a similar phase space graph at stability limit, using the analytical field model FFAG-SPI.

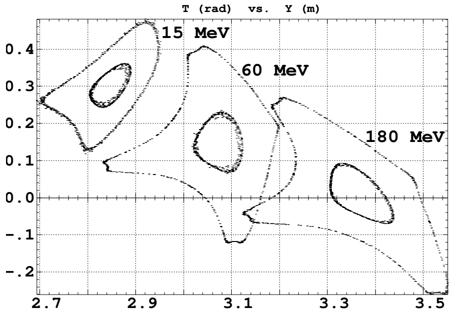

Fig. 11.15 Radial motion stability limits at three different energies, with either zero Z-motion (outer limits) or very small initial Z-motion (inner limits): non-linear coupling is responsible for the reduction of the dynamical acceptance

11.12 Dynamic Aperture

Extend the previous stability limit search (exercise 11.11) to produce the dynamic aperture in (Y,Z) space, at 15, 57 and 180 MeV.

11.13 Bucket height, Synchrotron Tune

Check the value of the synchrotron wave number (Eq. 8.4) and of the momentum acceptance (Eq. 8.6),

(a) in stationary bucket mode (synchronous phase $\phi_s = 0$), at 15 and 180 MeV,

(b) in accelerating bucket mode (say, synchronous phase $\phi_s = 30$ deg).

11.14 Acceleration, Transverse Betatron Damping

Produce a simulation of a 15 → 180 MeV acceleration cycle in RACCAM ring, for a single particle with paraxial radial and axial motions. Take an acceleration rate of 10 kVolts per turn. Acceleration uses CAVITE[IOPT=6], which imposes defining the particle type, with PARTICUL; multiturn is obtained using REBELOTE. SCALING takes care of having magnetic fields ramped to follow the momentum boost by CAVITE.

Show the betatron damping, graphically, check Eqs. 11.21, 11.22.

11.3.3 FFAG Acceleration Methods

Regarding the lattice, the following three exercises are based on a very similar radial sector triplet FFAG to that studied in detail in the Sect. 11.3.1 exercise series. Thus earlier simulation input data files can be used here, and will only require minor adaptations.

Regarding beam acceleration, the input data files and methods developed in the previous exercises (exercises 11.5, 11.13, 11.14) can be used to set up the present acceleration simulation input data.

11.15 Hybrid Acceleration

Produce a simulation of hybrid acceleration in the 35 keV→ 7 MeV, C^{4+}, FFAG injector addressed in Ref. [27, Slides 17-18]. It is suggested to proceed with staged simulations in the following order:

(a) Build the input data file for a $k = 0.7$, radial sector DFD cell, and subsequently for an 8-cell ring. The methods of the exercises in Sect. 11.3.1 can be used to construct the cell.

(b) Add acceleration, using a single, 5 kV RF cavity, simulated using CAVITE;

(c) add betatron-style acceleration, using CAVITE[IOPT], with proper choice of IOPT option.

11.16 Bucket Acceleration

Produce a simulation of bucket acceleration of a short-lived muon bunch, from 3.6 to 12.6 GeV, following Ref. [13, pp. 4507-4508]. It is suggested to proceed with staged simulations in the following order:

(a) Set up a 225-cell, k=1390, DFD ring. The methods of the exercises in Sect. 11.3.1 can be used to construct the cell.

(b) Add acceleration, 1.8 GV per turn, using 225 (one per cell), 8 MV, 200 MHz RF cavities, harmonic h=675. Re-produce Figs. 5, 6 of Ref. [13, p. 4508].

(c) Add in-flight decay (MCDESINT keyword): give the muon survival rate over the acceleration cycle. Check against theory.

11.17 Serpentine Acceleration

Produce a simulation of 0.38 to 1.1 GeV serpentine acceleration, following Ref. [12]. It is suggested to proceed with staged simulations in the following sequence:

(a) Set up a 225-cell, k=1390, DFD ring. The methods of the exercises in Sect. 11.3.1 can be used to construct the cell.

(b) Add acceleration, using a single, 60 MV RF cavity, harmonic h=10. Reproduce Figs. 5, 6 of Ref. [13, p. 4508].

References

1. Cole, F. T.: O Camelot, a Memoir of the MURA Years. Cyclotron Conference, East Lansing, USA, May 13-17, 2001. https://accelconf.web.cern.ch/accelconf/c01/cyc2001/extra/Cole.pdf
2. Kolomensky A. A., et al.: Some questions of the theory of cyclic accelerators. Ed. AN SSR, 1955, p. 7, PTE, No 2, 26 (1956)
3. Symon, K. R. Phys. Rev 100, 1247 (1955) Symon, K.R., et al.: D. W. Kerst, L. W. Jones, L. J. Laslett, and K. M. Terwilliger, Fixed-Field Alternating-Gradient Particle Accelerators. Phys. Rev. 103, 1837 (1956)
4. Ohkawa, T.: Two-beam fixed field alternating gradient accelerator. Rev. Sci. Instrum. 29, 108 (1958)
5. Machida, Shinji: Muon (FFAG) Accelerators. THYAB01 talk; PAC 2007 Accel. Conf., June 25-29, 2007, Albuquerque, NM, USA. https://accelconf.web.cern.ch/p07/TALKS/THYAB01_TALK.PDF. Copyrights under license CC-BY-3.0, https://creativecommons.org/licenses/by/3.0; no change to the material
6. Mori, Y.: Developments of FFAG accelerator. 17th international conference on cyclotrons and their applications 2004, Tokyo (Japan), 18-22 Oct 2004. https://www.osti.gov/etdeweb/biblio/20676358
7. Craddock, M.: The rebirth of the FFAG. CERN Courrier (27 July 2004). https://cerncourier.com/a/the-rebirth-of-the-ffag/
8. Collot, J.: The rise of the FFAG. CERN Courrier (19 August 2008). https://cerncourier.com/a/the-rise-of-the-ffag/
9. Ishi, Y.: Status of KURRI Facility. Proceedings of the FFAG 2016 workshop, Imperial college, London, 2016. https://indico.cern.ch/event/543264/contributions/2295846/attachments/1333675/2005286/FFAG16_LONDON_ishi.pdf
10. Pyeon, C.H., et al.: First injection of spallation neutrons generated by high-energy protons into the Kyoto University critical assembly. J. Nucl. Sci. Technol. 46, 1091 (2009)
11. Méot, F.: A Multiple-Room, Continuous Beam Delivery, Hadron-Therapy Installation. Physics Procedia 66 (2015) 361-369. https://www.sciencedirect.com/science/article/pii/S1875389215001984
12. Yamakawa, E., et al.: Serpentine acceleration in zero-chromatic FFAG accelerators. Nuclear Instruments and Methods in Physics Research Section A, Volume 716, 11 July 2013, Pages 46-53
13. Planche, T., et al.: New Approaches to Muon Acceleration With Zero-Chromatic FFAGs. THPD093, Proceedings of IPACâĂŹ10, Kyoto, Japan (2010). http://accelconf.web.cern.ch/AccelConf/IPAC10/papers/thpd093.pdf
14. Plache, T., et al.: New approaches to muon acceleration with zero-chromatic FFAGs. THPD093, Proceedings of IPACâĂŹ10, Kyoto, Japan. https://accelconf.web.cern.ch/IPAC10/papers/thpd093.pdf
15. Mori, Y., et al.: Multi-beam acceleration in FFAG synchrotron. Proc. PAC 2001 Accel. Conf. 588-590 (2001). http://accelconf.web.cern.ch/AccelConf/p01/PAPERS/ROPA010.PDF
16. Sato, A., et al.: FFAG as Phase Rotator for the PRISM Project. Proc. EPAC 2004 Accel. Conf. 713-715 (2004). http://accelconf.web.cern.ch/AccelConf/e04/PAPERS/MOPLT070.PDF
17. Haj Tahar, M., Méot, F.: Tune compensation in nearly scaling fixed field alternating gradient accelerators. Physical Review Accelerators and Beams 23, 054003 (2020). https://journals.aps.org/prab/abstract/10.1103/PhysRevAccelBeams.23.054003
18. Tanigaki, M., et al.: Construction of FFAG accelerators in KURRI for ADS study. Proc. EPAC 2004 Accel. Conf., 2676-2678 (2004). http://accelconf.web.cern.ch/accelconf/e04/PAPERS/THPLT078.PDF

19. Neuvéglise, D, Méot, F.: An alternative design for the RACCAM magnet with distributed conductor. FR5REP095, Proc. PAC09 Conf., 5002-5004, Vancouver, BC, Canada (2009). https://accelconf.web.cern.ch/PAC2009/papers/fr5rep095.pdf
20. Planche, T., et al.: Design of a prototype gap shaping spiral dipole for a variable energy proton therapy FFAG. NIMA 604 (2009) 435-442.
21. Aiba, M., et al.: Development of 150-MeV FFAG at KEK. FFAG03 Workshop, KEK, Japan, July 7-12,2003. http://130.246.92.181/FFAG/FFAG03_HP/plenary/mori1.pdf
22. Aiba, M., Méot, F., Determination of KEK 150 MeV FFAG parameters from ray-tracing in TOSCA field maps, CERN-NUFACT-NOTE-140 ; CARE-Note-2004-030-BENE ; CEA-DAPNIA-2004-188 - 2004. http://cds.cern.ch/record/806545/files/note-2004-030-BENE.pdf
23. Aiba, M.: Tracking study for FFAG. FFAG Accelerator Workshop; FFAG02, KEK, Tsukuba February 13-15, 2002. https://ffag.pp.rl.ac.uk/FFAG/FFAG02_HP/2002_02_13/20020213_M.Aiba.pdf
24. Antoine, S. et al.: Principle design of a proton therapy, rapid-cycling, variable energy spiral FFAG, NIM A 602 (2009) 293-305.
25. Fourrier, J., Martinache, F., Méot, F., Pasternak, J.: Spiral FFAG lattice design tools,application to 6-D tracking in a proton-therapy class lattice. NIM A 589 (2008) 133-142.
26. Méot, F.: RACCAM: a status including magnet prototyping and magnetic measurements. International conference on FFAGs, Fermilab, 21-25 September 2009. https://indico.fnal.gov/event/2672/session/2/contribution/8/material/slides/
27. Tanaka, H.: Feasibility Study of Hybrid Accelerator and Superconducting FFAG. FFAG04 Accelerator Workshop, KEK, Tsukuba (October 13-16, 2004). http://130.246.92.181/FFAG/FFAG04_HP/index.html
28. Tanaka, H., et al.: Hybrid Accelerator Using an FFAG Injection Scheme. Cyclotrons 2004 Conf., Tokyo, Japan (18-22 Oct 2004). http://accelconf.web.cern.ch/AccelConf/c04/data/CYC2004_papers/19C6.pdf
29. Haj Tahar, M.: High Power Ring Methods and Accelerator Driven Subcritical Reactor Application. PhD thesis dissertation, BNL and University Grenoble-Alpes (Jan. 2017). https://www.bnl.gov/isd/documents/94721.pdf
30. Méot, F., Lemuet, F.: Developments in the ray-tracing code Zgoubi for 6-D multiturn tracking in FFAG rings. NIM A 547 (2005) 638-651.
31. Méot, F.: Zgoubi Users' Guide. https://www.osti.gov/biblio/1062013-zgoubi-users-guide An up-to-date version of the guide: https://sourceforge.net/p/zgoubi/code/HEAD/tree/trunk/guide/Zgoubi.pdf